Regional PM$_{2.5}$ pollution confined by atmospheric internal boundaries in the North China Plain: boundary layer structures and numerical simulation

Xipeng Jin[1], Xuhui Cai[1]*, Mingyuan Yu[2], Yu Song[1], Xuesong Wang[1], Hongsheng Zhang[3], Tong Zhu[1]

[1]College of Environmental Sciences and Engineering, State Key Lab of Environmental Simulation and Pollution Control, Peking University, Beijing 100871, China

[2]School of Applied Meteorology, Nanjing University of Information Science and Technology, Nanjing 210044, China

[3]Department of Atmospheric and Oceanic Sciences, School of Physics, Peking University, Beijing 100871, China

Correspondence to: Xuhui Cai (E-mail: xhcai@pku.edu.cn)

1 **Abstract.** This study reveals mesoscale planetary boundary layer (PBL) structures under various

2 pollution categories during autumn and winter in the North China Plain. The role of the atmospheric

3 internal boundaries (AIBs, referring to the discontinuity of meteorological conditions in the lateral

4 direction) in regulating PBL structure and shaping the PM$_{2.5}$ pollution patterns is emphasized. The

5 Weather Research and Forecast model is used to display the three-dimensional meteorological fields, and

6 its performance is evaluated by surface observations and intensive soundings. The evaluation

7 demonstrates that the model reasonably captures the mesoscale processes and the corresponding PBL

8 structures. Based on the reliable simulations, three typical pollution cases are analyzed. Case-1 and Case-

9 2 represent the two main modes of the wind shear category pollution, which is featured with airflow

10 convergence line/zone as AIB and thus is dominated by dynamic effect. Case-1 presents the west-

11 southwest wind shear mode associated with a trough convergence belt. The convergent airflow layer is

12 comparable to the vertical scale of the PBL, allowing PM$_{2.5}$ accumulation to form a high pollution area.

13 Case-2 exhibits another mode with south-north wind shear. A "lying Y-shaped" convergence zone is

14 formed with a thickness of about 3000m, extending beyond the PBL. It defines a clear edge between the

15 southern polluted airmass and the clean air in the north. Case-3 represents the topographic obstruction

16 category, which is characterized by a cold-air damming AIB in front of the mountains. The PBL at the

17 foothills is thermally stable and dynamically stagnant due to the capping inversion and the convergent

18 winds. It is in sharp contrast to the well-mixed/ventilated PBL in the southern plains, especially in the

19 afternoon. At night, this meteorological discontinuity becomes less pronounced. The diurnal variation of

20 the PBL thermal-dynamic structure causes the pollutants to concentrate at the foot of the mountains

during the daytime and locally accumulate throughout the entire plain in the evening. These results provide a more complete mesoscale view of the PBL structure and highlight its spatial heterogeneity, which promotes the understanding of air pollution at the regional scale.

Keywords: Boundary layer structure; atmospheric internal boundaries; $PM_{2.5}$; modeling

1 Introduction

The planetary boundary layer (PBL) is the lowest section of the atmosphere that responds directly to the heat and friction from the Earth's surface (Stull, 1988; Garratt, 1992). Most air pollutants are intensively emitted or chemically produced within this layer, and their horizontal transport and vertical mixing are affected by the dynamic flow and thermal stability of the PBL (Tennekes, 1974). Therefore, the PBL structure plays a crucial role in the evolution, magnitude and distribution of air pollution.

The PBL structure has been recognized to be strongly dependent on three categories of factors: (i) the single-column vertical property (such as turbulence intensity) forced by the local surface's energy balance; (ii) the lateral-section horizontal variation of wind, temperature and humidity regulated by the mesoscale meteorological process and (iii) the three-dimensional spatial evolution controlled by the large-scale synoptic system (Boutle et al., 2010). The local vertical PBL structure and its impact on air pollution have been widely discussed from different aspects including turbulent mixing (Emeis and Schafer, 2006; Ren et al., 2019), dynamic effect (Dupont et al., 2016), entrainment (Li et al., 2018; Jin et al., 2020), and radiative feedback with aerosol (Petaja et al., 2016). In these studies, the PBL height at a certain site has been the most commonly used indicator to analyze the correlation with pollutant concentration, whether from the time scale of the diurnal cycle, daily variation, or longer period (Bianco et al., 2011; Liu et al., 2019; Miao and Liu, 2019). Moreover, some studies investigate the PBL spatial structure under the large-scale force of weather systems (Prezerakos, 1998; Boutle et al., 2010; Mayfield and Fochesatto, 2013). Sinclair et al. (2010) report the three-dimensional PBL structure developed beneath an idealized mid-latitude weather system, which is characterized by a deep convective PBL in the eastern flanks of the anticyclone and a shallow shear-driven PBL in the cyclone's warm sector. The effect of the monsoon trough on the PBL has also been indicated, showing relatively low PBL capped by a stable layer in the western end of the trough line, while a well-defined deep moist layer with active thermal instability in the eastern end (Rajkumar et al., 1994; Narasimha, 1997; Potty et al., 2001). In recent years, synoptic classification has been used to explore the role of different weather circulations on PBL structure and to further analyze air pollution (Peng et al., 2016; Xiao et al., 2020). The movement of the synoptic systems makes the shallow and deep boundary layers develop alternately in a certain area, regulating the periodic evolution of large-scale air pollution.

As the intermediate scale, mesoscale systems interact with PBL in more direct and complex ways,

since they occur in the lower troposphere with vertical extension comparable with the PBL depth and horizontal scale close to the regional range. Discontinuity of meteorological properties inside and outside these systems presents as atmospheric internal boundaries (AIBs) in the lateral direction, usually manifested as temperature contrast and/or wind shift. Previous studies have emphasized their influence on the initiation of convective storms (Sanders and Doswell, 1995; Hane et al., 2002; Bluestein, 2008). On the other side, as internal lateral boundaries within the low-level atmosphere, the AIBs can lead to the abrupt change of the PBL spatial structure, which is of particular importance to the evolution of regional pollution. The effects of mesoscale sea-land and mountain-valley circulations on the PBL have been clarified, i.e., the thermal internal boundary layer in the coastal area and the depressed PBL close to a mountain base (Garratt, 1990; Lu and Turco, 1995; Talbot et al., 2007; De wekker, 2008; Miao et al., 2015). Some studies discuss the PBL structure under the rule of other types of mesoscale/sub-synoptic scale systems, such as the persistent cold-air pools in the Salt Lake valley (Lareau et al., 2013), foehn winds in the Eastern Alps (Seibert, 1990; Baumann et al., 2001), and leeside troughs and cold-air damming around the Appalachian mountains (Seaman and Michelson, 2000; Bell and Bosart, 1988), as well as the frequent cold and warm fronts in Europe (Berger and Friehe, 1995; Sinclair, 2013). However, there needs more understanding of their impact on the evolution of air pollution.

The North China Plain (NCP) is one of the most polluted areas in the world. The dense population and developed industries produce intensive emissions in this region, with most sources located in the plain area and less in the northern and western mountains (their spatial distribution is presented in the supplement material). High-intensity primary emissions are the fundamental cause of air pollution, which directly releases pollutants into the atmosphere and provides precursors for secondary aerosol formation (Lyu et al., 2016; Zhao et al., 2019). In order to improve the air quality, a series of stringent emission reduction policies are implemented from 2013, which make the annual mean $PM_{2.5}$ concentrations decrease by 32% in 2017 (Zhang et al, 2019). However, the severe polluted days still occur frequently, especially in winter (Zhang et al., 2018). During these pollution episodes, adverse meteorological conditions are the dominant factors causing high pollution levels and various spatial patterns, as there are no significant changes in emissions in a short period (e.g., weeks). Extensive studies have been conducted to investigate the meteorological causes of regional pollution in the NCP, such as the local meteorological factors and large-scale synoptic process (Ye et al., 2016; Ren et al., 2019; Li et al., 2020). Nevertheless, the knowledge about the PBL spatial structures under the impact of the mesoscale AIBs is still insufficient, and the role of the special PBL structures plays in the air pollution evolution at a regional scale is even unclear (Bluestein, 2008; McNider and Pour-Biazar, 2020).
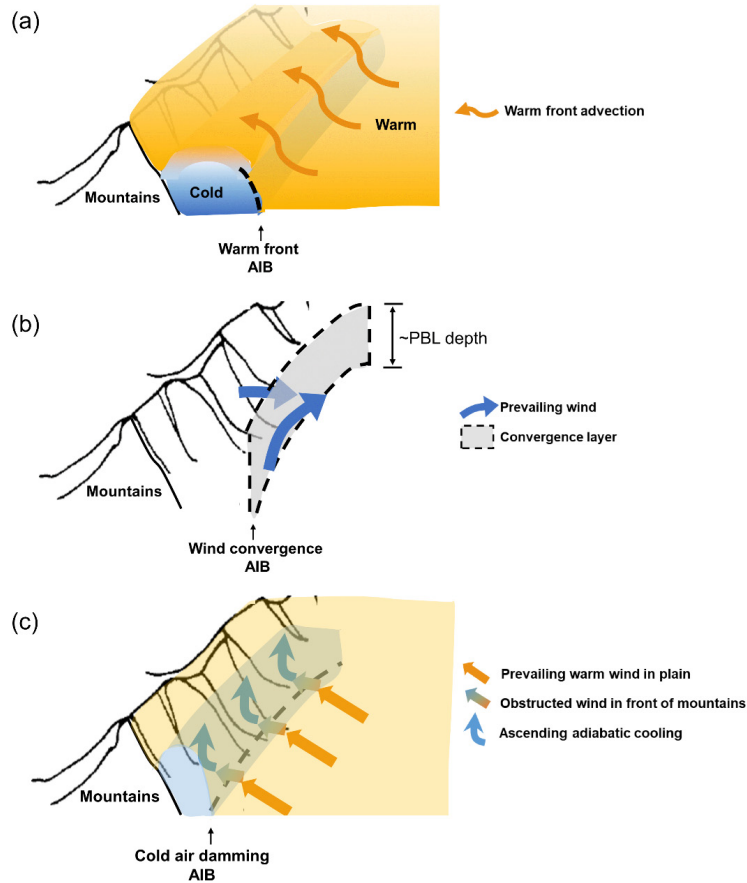
86

87 Figure 1. Schematic diagram showing the conceptual model of PBL spatial structures under three

88 pollution categories. (a) Frontal category: the blue-shaded and orange-filled areas represent the isolated

89 and stable cold air mass ahead of the warm front and the warmer well-mixing atmosphere behind the

90 front. The orange arrows indicate warm front advection. (b) Wind shear category: two blue arrows

91 represent the airflows ahead of and behind the trough. The gray-filled area indicates the dynamic

92 convergence layer with a depth comparable to the boundary layer height. (c) Topographic obstruction

93 category: the light blue filled area indicates the cold air damming at the foot of the windward mountains.

94 Terrain obstruction disrupts the geostrophic balance so that the southerly warm advection weakens (long

95 orange arrows) and turns to the easterly cold advection (short gradient-color arrows), and meanwhile, the

96 air mass accumulates to produce a lift cooling (up blue arrows). Black dashed lines in (a-c) indicate the

97 warm front AIB, wind convergence AIB, and cold air damming AIB respectively. The PBL spatial

98 structure under the first category has been revealed by Jin et al. (2021). For the latter two categories, their

99 PBL three-dimension structures are discussed in Sect 3.3 in this paper.

100 Based on the surface observations, a thorough survey of the $PM_{2.5}$ pollution categories under the

101 control of the AIBs is carried out by Jin et al. (2022, submitted). It is found that the pollution formation-

102 maintenance process in the NCP can be classified into three categories, i.e., the frontal category, wind

103 shear category and topographic obstruction category during the autumn and winter of the investigated 7

years (2014–2020). Figure 1 shows the schematic diagram of three pollution categories corresponding to various AIBs. The frontal category represents about 41 % of all 98 pollution episodes, and its PBL spatial structure has been revealed in a previous case study (Jin et al., 2021). It is characterized by an isolated cold air mass, which is laterally confined by mountains and warm front AIB, and vertically covered by a warm dome (Fig. 1a). The strong elevated inversion depresses the PBL height abruptly to 200~300 m within the cold area in contrast to 600~800 m outside the zone, constituting adverse dispersion conditions and resulting in the most serious $PM_{2.5}$ pollution. The wind shear category is associated with airflow convergence AIB (Fig. 1b), which is dominated by dynamic effect and causes lighter $PM_{2.5}$ pollution. West-southwest wind shear and south-north wind shear are the two main modes. The third category occurs when the airflow cannot cross the topographic obstruction and form the cold air damming AIB. A cold and heavy pollution belt develops at the foot of the windward mountains (Fig. 1c), under the synergistic effect of dynamical obstruction and thermal stratification. Although previous studies have classified the air pollution and revealed the spatial characteristics of the first category, the three-dimensional PBL structures interacted with AIBs under the other two categories are not yet clarified, which is responsible for 43% of pollution episodes in the NCP. In order to fulfill this knowledge gap, the present study deeply analyzes representative cases of wind shear category and topographic obstruction category (Detailed analyses in Sect 3.3), and finally provides a complete conceptual model of the PBL spatial structure in the NCP under various pollution categories and corresponding AIBs (Fig.1).

The mesoscale meteorological models, such as the Weather Research and Forecast (WRF) with the high spatial and temporal resolution, are plausible tools to capture the mesoscale systems and display detailed spatial structures in the lower atmosphere, including the AIBs and the PBL (Jimenez et al., 2016, Pielke and Uliasz, 1998; Seaman, 2000; Hanna and Yang, 2001; McNider and Pour-Biazar, 2020). The present study aims to reveal the thermal and dynamic structures of the PBL and their evolution associated with different AIBs in the condition of pollution episodes, by using the WRF model. For this purpose, the model performance is at first evaluated with detailed sounding data from intensive experiments, to ensure the model's ability in reproducing the meteorological fields and their three-dimensional structures in the concerned region. The article is organized as follows. The following section describes the PBL sounding observations as well as the WRF model settings. Section 3 provides an overview of representative pollution cases and the evaluation of the model performance. Furthermore, the PBL spatial structures under various pollution categories are analyzed. Finally, the conclusions are presented and the uncertainty of the mesoscale meteorological model is discussed in Sect. 4.

2 Data and methods

2.1 Observations and data analysis

Intensive GPS (Global Positioning System) sounding data: Two periods of field experiments were carried out to evaluate the meteorological model and explore wintertime PBL structure in the NCP: at Cangzhou (38°13′ N, 117°48′ E, Fig. 2a) from January 8 to 28, 2016 and at Dezhou (37°16′ N, 116°43′ E, Fig. 2a) from December 25, 2017, to January 24, 2018. GPS radiosonde (Beijing Changzhi Sci & Tech Co. Ltd., China) was used to obtain profiles of wind speed, wind direction, temperature, and relative humidity with a vertical resolution of approximately 1 s (3~5 m). Eight soundings were taken on each day, at 0200, 0500, 0800, 1100, 1400, 1700, 2000 and 2300 LT (i.e., Local Time = Universal Time Coordinated + 8). The reliability of the GPS sounding data has been systematically evaluated by Li et al. (2020) and Jin et al. (2020, 2021).

Routine radiosonde sounding data: Routine sounding data from the meteorological station of Beijing (39°56′ N, 116°17′ E, Fig. 2a) were collected during October 7–12, 2014, in the absence of intensive PBL observation. The data were obtained from Wyoming University, USA (http://weather.uwyo.edu.html), and the original observation data with higher vertical resolution were provided by the China Meteorological Administration. The routine soundings were taken 2 times a day, at 0800 and 2000 LT.
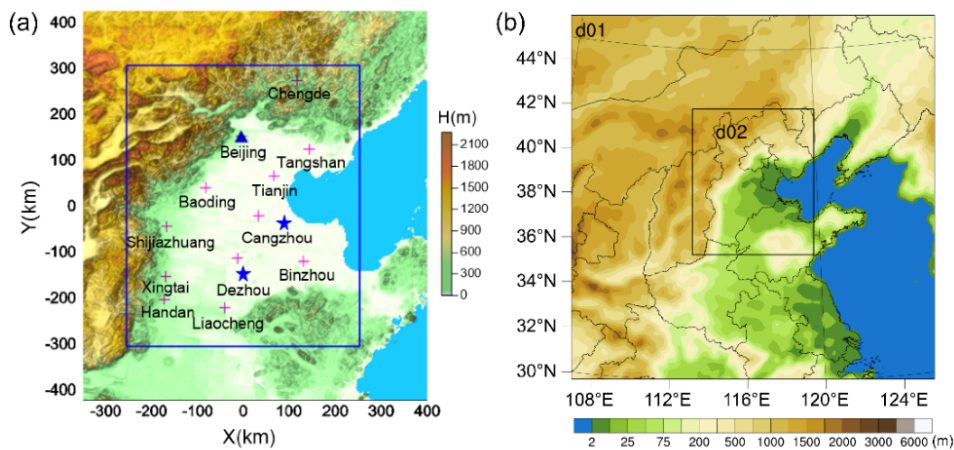
Figure 2. Geographical map of the (a) observation area and (b) WRF model domain. Intensive GPS soundings at Dezhou and Cangzhou (star), routine radiosonde sounding at Beijing (triangle) and air quality stations (plus) are indicated in (a). The rectangle in (a) is the same as the model inner domain d02 in (b).

PBL height and vertical profiles: During the two periods of intensive field experiments, 160 and 240 datasets were collected at these two sites, including vertical profiles of temperature, relative humidity, wind speed, and wind direction. We carried out quality control on the original sounding data and

eliminated outliers and then calculated the profiles of potential temperature. All the profiles were smoothed by a three-point moving average method and were interpolated to obtain a vertical resolution of 10 m. The PBL height was derived via the potential temperature profile method and the detailed calculation followed the mathematical method established by Liu and Liang (2010). Sounding data were used to evaluate the model performance and to analyze the three-dimensional thermal and dynamic spatial structure of the PBL.

In addition to the PBL sounding data, the routine meteorological observation and air quality monitoring data were used to obtain the surface meteorological field and pollutant concentration field. The spatial distributions of sea level pressure, 10 m wind vector, potential temperature, and the corresponding $PM_{2.5}$ concentration were obtained by data interpolation or diagnostic model, details of the methods were referred to Jin et al. (2021).

2.2 Model simulations

The WRF model was used to investigate the vertical and horizontal structures of the PBL. Two nested domains (Fig. 2b) were employed with horizontal grid resolutions of 15 and 5 km. Each domain had 37 vertical layers extending from the surface to 100 hPa, with 25 layers within 2 km (with the respective height of about 9 m, 25 m, 50 m, 85 m, 120 m, 160 m, 200 m, 240 m, 290 m, 350 m, 420 m, 500 m, 580 m, 660 m, 740 m, 820 m, 900 m, 980 m, 1080 m, 1200 m, 1350 m, 1550 m, 1700m, 1850 m, and 2000 m) to resolve the PBL structure. The meteorological initial and boundary conditions were set using the United States National Center for Environmental Prediction Final Analysis (NCEP-FNL) dataset. The physics parameterization schemes applied in this study were the same as Jin et al. (2021).

2.3 Representative cases

As mentioned above, $PM_{2.5}$ pollution episodes in the NCP are identified in the frontal category, wind shear category, and topographic obstruction category, according to their association with the mesoscale AIBs (Jin et al., 2022 submitted). The present study tries to reveal the PBL structures modified by the AIBs under various pollution categories. Among them, the first category has been investigated previously (Jin et al., 2021). We focus on the representative cases under the other two categories in this paper. For the wind shear category, there are two main shear modes: west-southwest wind shear and south-north wind shear. Therefore a total of three typical cases are selected to respectively represent these two pollution categories, i.e., Case-1 for west-southwest wind shear mode: during January 17–21, 2018; Case-2 for south-north wind shear mode: during January 7–11, 2016; and Case-3 for topographic obstruction category: during October 7–12, 2014. The temporal and spatial evolution of their $PM_{2.5}$ concentrations and the corresponding surface meteorological conditions would be analyzed based on routine observations, and their PBL spatial structures would be revealed by the WRF model simulations.

3 Results

3.1 Basic features of the cases

The surface observations for these three cases are presented firstly. According to the temporal evolution of $PM_{2.5}$ concentration at different stations in the NCP (Fig. 3), all of these three pollution episodes went through the stages of formation, maintenance and diffusion. As shown in Fig. 3a, Case-1 was characterized by two main concentration peaks (300 μg m^{-3} at Handan vs 500 μg m^{-3} at Cangzhou) in the formation-maintenance stage (January 17–20, 2018), with the latter being higher than the former. From noon on January 20, 2018, pollution in Tianjin-Cangzhou-Shijiazhuang diffused successively and all sites reached a clean level on the afternoon of January 21, 2018. For Case-2, the pollution formed in the first two days, maintained over the next day and was cleaned on the night of January 10, 2016 (Fig. 3b). The southern sites such as Liaocheng and Dezhou were the most polluted (reaching 450 μg m^{-3}) and the northern cities such as Beijing and Chengde were the least polluted (less than 150 μg m^{-3}). Pollution in Case-3 experienced the formation process on October 7–8, 2014, maintained for the successive three days, and ended on October 12, 2014 (Fig. 3c). During this period, the piedmont sites (Baoding, Beijing and Shijiazhuang) kept always a high concentration regardless of day and night (about 400 μg m^{-3}), while the southeast sites (Binzhou, Dezhou and Cangzhou) had lighter pollution and obvious diurnal cycle (lower than 250 μg m^{-3}).

The spatial patterns of $PM_{2.5}$ pollution, from the formation (Fig. 4i), maintenance (Fig. 4ii-iv), to the diffusion stage (Fig. 4v), are illustrated for each case. In the formation stage, the polluted air mass of Case-1 and Case-3 built up along the mountains from the southwest of the NCP, with the latter being more concentrated and the former spreading southwestward (Fig. 4a-i, c-i). While the pollution in Case-2 first developed from the south (Fig. 4b-i). During the pollution maintenance process, Case-1 was featured with widespread $PM_{2.5}$ flooding the NCP, making the eastern region gradually covered by heavy pollution (Fig. 4a, ii-iv); in Case-2, a polluted air mass has been advancing northward with a clear edge, but it did not reach the northern mountainous area (Fig. 4b, ii-iv); the spatial distribution of $PM_{2.5}$ of Case-3 was characterized by the day-night contrast, manifested as pollution filling the entire plain area at night while concentrating in front of the mountains with a distinct edge on the southeast side during the daytime (Fig. 4c, ii-iv). Finally, these pollution cases were diffused in different ways. In Case-1, the clean air first occupied the northern parts of the NCP with a large concentration gradient on the front edges (Fig. 4a, v). As for Case-2, $PM_{2.5}$ was restored to a clean level from the northeast (Fig. 4b, v). Pollution in the northwest was earliest removed in Case-3, with Beijing acting like a loophole/passageway in the cleaning process (Fig. 4c, v). These cases presented various pollution distributions, however, all of them were characterized by clear edges or distinct heavy pollution cores.
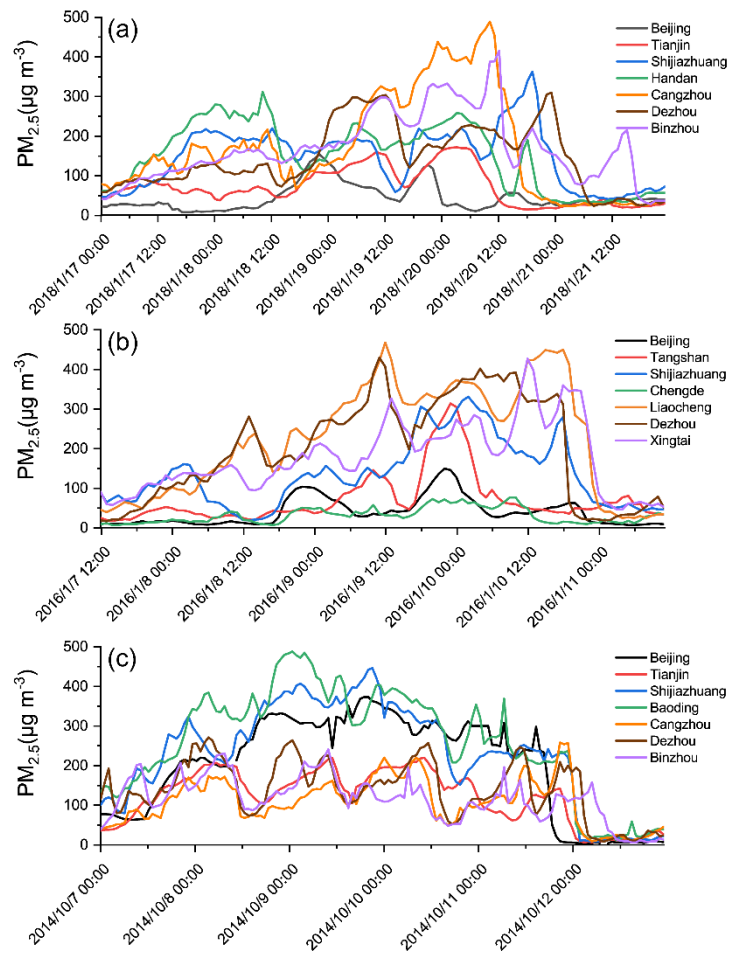
226
227 Figure 3. Temporal evolution of PM$_{2.5}$ concentrations during Case1–3, respectively represent (a) west-
228 southwest wind shear mode (January 17–21, 2018), (b) south-north wind shear mode (January 7–11,
229 2016), and (c) topographic obstruction category (October 7–12, 2014). The locations of these PM$_{2.5}$
230 stations are marked in Fig. 2a.

231
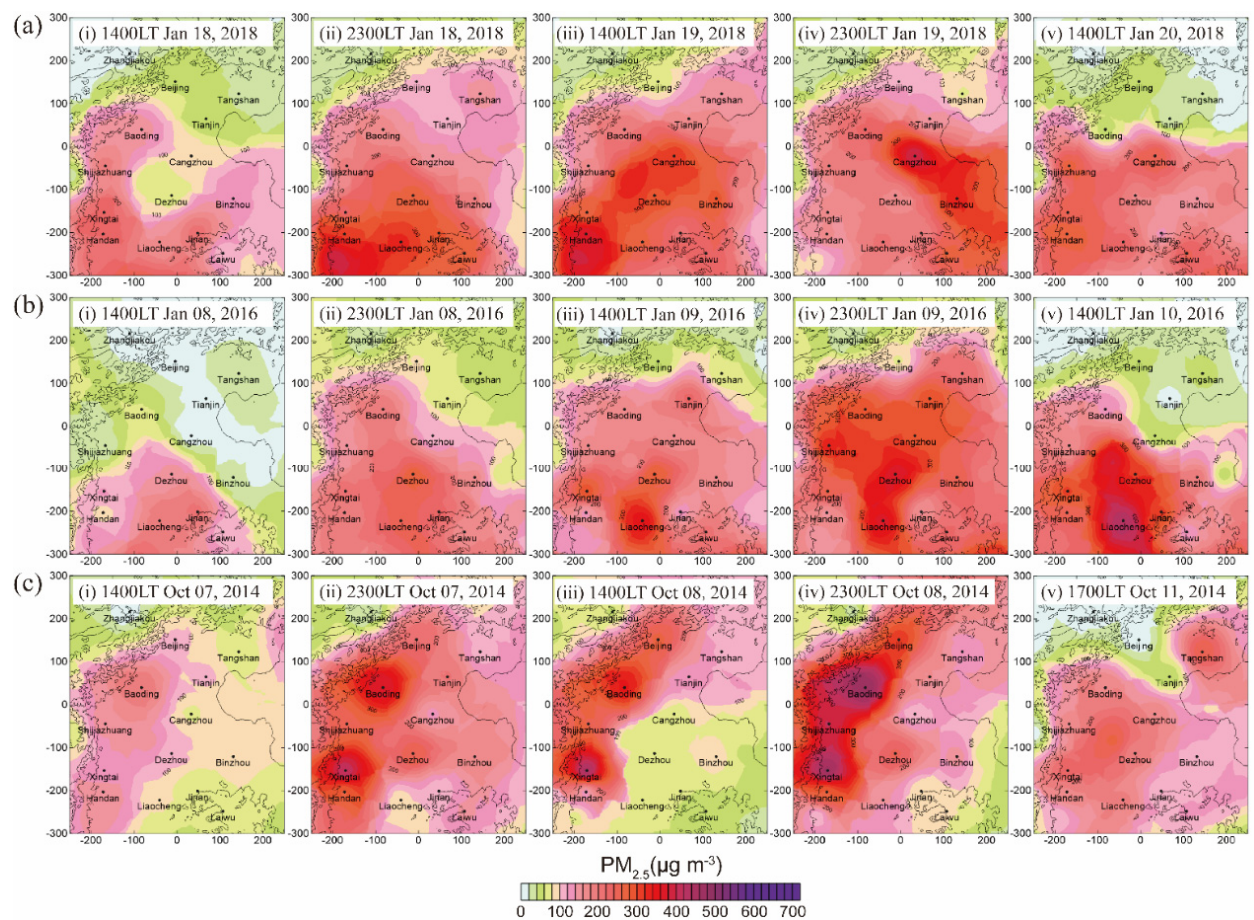
Figure 4. Spatial distributions of observed surface PM$_{2.5}$ concentrations (shaded colors) at the pollution stages of (i) formation, (ii-iv) maintenance, and (v) diffusion during

representative Case1–3 under (a) west-southwest wind shear mode, (b) south-north wind shear mode, and (c) topographic obstruction category. Values shown in x- and y-axis

denote the distances (km) to the domain center. The PM$_{2.5}$ concentration fields are derived from spatial interpolation of pollution observed data at monitoring stations.
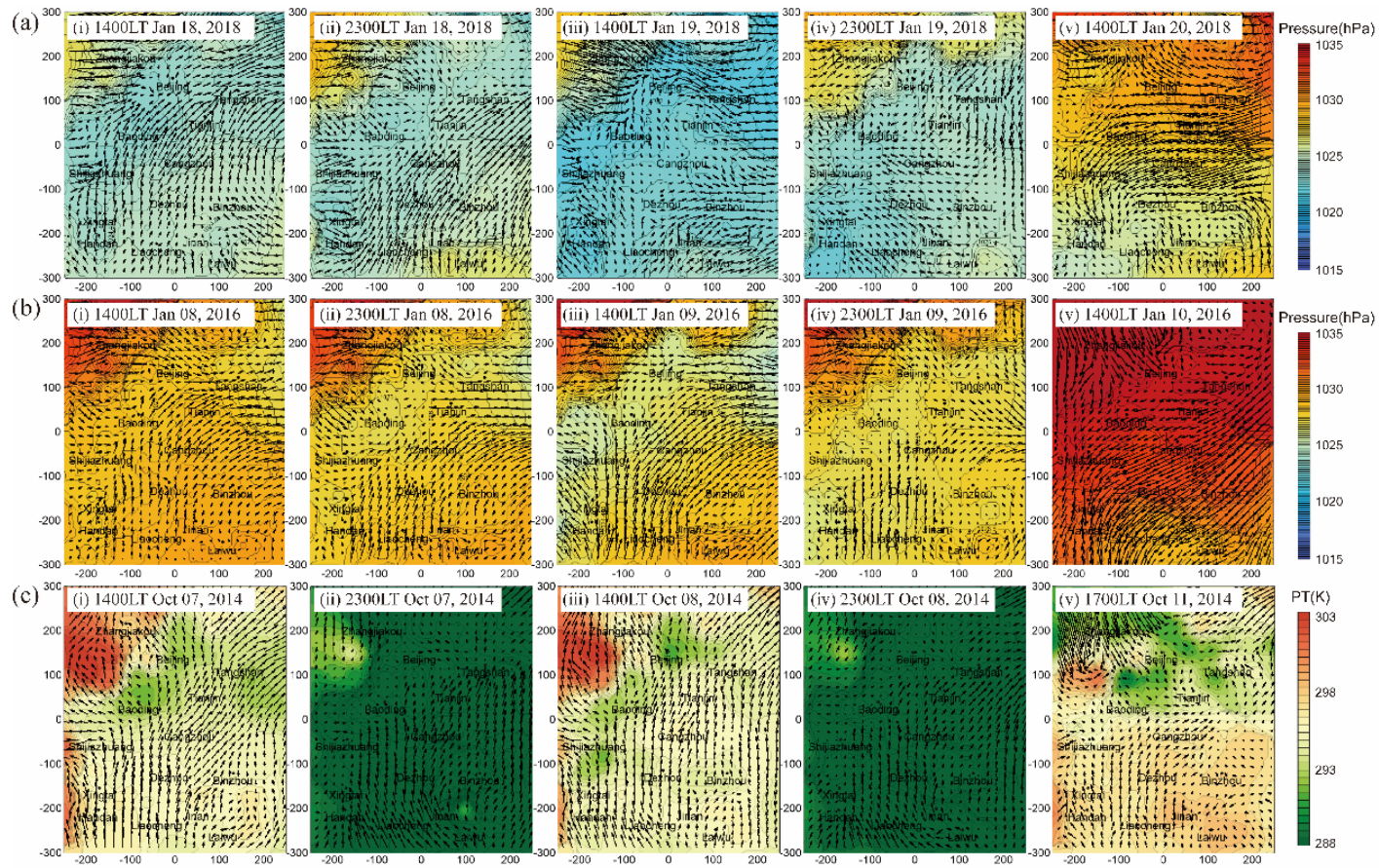
Figure 5. Observed sea level pressure/potential temperature and wind vectors at the pollution stages of (i) formation, (ii-iv) maintenance, and (v) diffusion during representative Case1–3 under (a) west-southwest wind shear mode, (b) south-north wind shear mode, and (c) topographic obstruction category. The shaded colors represent the sea level pressure in (a-b) and the potential temperature in (c). The arrows indicate wind vectors. Values shown in x- and y-axis denote the distances (km) to the domain center.

239   The correspondent surface meteorological fields of the three cases are shown in Fig. 5. Case-1 and

240   Case-2 are the two main modes of wind-shear category, for which dynamic AIB plays a dominant role,

241   and thus the observed sea level pressure and wind fields are discussed (Fig. 5a-b). Case-3 belongs to the

242   topographic obstruction category affected by the AIB created by the cold air damming, and its potential

243   temperature and wind fields are displayed to focus on the combined action of the thermal and dynamic

244   properties (Fig. 5c). As shown in Fig. 5a, i-iii, the pollution formation and maintenance processes of

245   Case-1 were dominated by a leeward trough, which induced the westerly airflow shear to the southwest

246   wind and produced a convergence belt at the trough axis. As the trough broadened and moved eastward,

247   the wind convergence zone also moved (Fig. 5a, i-iii). On the evening of January 19, 2018, the leeward

248   trough temporarily evolved into an inverted trough under the force of the approaching high-pressure,

249   creating a cyclonic convergence (Fig. 5a, iv). This explains why the heavy pollution expands eastward

250   in this episode (refer to Fig. 4a, i-iv). Until January 20, 2018, a high-pressure system invaded the NCP

251   from the northeast, bringing strong northeast winds (Fig. 5a, v), which made the pollution disperse

252   southward in turn (refer to Fig. 4a, v). During Case-2, a saddle-shaped pressure field persisted in the

253   pollution formation-maintenance stage and induced the prevailing northerly winds in the northern NCP

254   against the dominant southerly flows in the southern area (Fig. 5b, i-iv). As a result, the polluted air mass

255   was prevented from advancing northward to the mountains, causing a strong contrast in pollution

256   concentration between the northern and southern parts of the domain (refer to Fig. 4b i-iv). Its pollution

257   diffusion process was also associated with a northeast high-pressure system, by strong northeasterly

258   airflows cleaning up the $PM_{2.5}$ (Fig. 5b, v). As for the Case-3 under the topographic obstruction category,

259   there was a narrow area with low potential temperature and weak southerly wind at the foot of the

260   mountains on the windward side in the daytime, but this feature became fuzzy at night (Fig. 5c, i-iv).

261   This diurnal variation repeatedly occurred during the formation and maintenance stage, which

262   corresponded excellently to the day-night difference in pollution distribution (refer to Fig. 4c i-iv). In the

263   end, the strong flows and cold air bursting like a jet stream through a pathway across Zhangjiakou-

264   Beijing-Tianjin (Fig. 5c, v), made pollutants begin to be swept out from the northwest (refer to Fig. 4c,

265   v).

3.2 Evaluation of simulated meteorological field

267   To reveal the PBL three-dimensional structure of these representative cases, numerical simulations

268   are conducted using the WRF model. It is necessary to evaluate the model reliability before analyzing

269   the simulated results. The model-observation comparisons in the previous studies usually focus on the

270   time series of surface meteorological elements, such as 10 m wind speed and direction, 2 m temperature

271   and humidity (Rogers et al., 2013; Bei et al., 2018; Qu et al., 2021). The model performance of their

272   spatial fields is often ignored, and the simulated PBL vertical structure is rarely evaluated. But the

regional distribution and vertical structure of wind, temperature, and humidity are crucial for air pollution. And of course, the PBL height is a key parameter in characterizing air pollution ventilation conditions. In this study, the evaluation is carried out from three perspectives: i) the temporal evolution and ii) the spatial pattern of near-surface potential temperature and wind speed, as well as iii) the vertical-temporal structure of these two variables at the sounding sites, in addition to the temporal variation of PBL height.

For the temporal evolution of the near-surface potential temperature and wind speed, the hourly observations and simulations of 13 key cities (Beijing, Tianjin, Shijiazhuang, Baoding, Handan, Tangshan, Cangzhou, Dezhou, Jinan, Weifang, Binzhou, Chengde and Zhangjiakou) evenly distributed in the NCP are compared during these three pollution cases. The model outputs are extracted from the grid points nearest to the observed sites. As shown in Table 1, the correlation coefficients of the simulated and observed hourly evolution of potential temperature and wind speed are 0.80~0.91 and 0.54~0.64 (p<0.01), respectively. In order to exclude the influence of the diurnal cycle on the correlation, the daily averages are also calculated and the obtained correlation coefficients are as high as 0.65~1 and 0.62~1 (p<0.01) for potential temperature and wind speed, respectively (Table S1). The statistical results demonstrate that the major variations in the time series of the surface observations are reproduced well by the model, which has also been recognized in previous studies (Rogers et al., 2013; Bei et al., 2018; Qu et al., 2021).

Table 1. Statistics of model performance for the hourly evolution of near-surface potential temperature and 10 m wind speed for selected 13 cities during the representative cases.

	Case-1				Case-2				Case-3			
	PT (K)		WS (m s^{-1})		PT (K)		WS (m s^{-1})		PT (K)		WS (m s^{-1})	
	R	RMSE	R	RMSE	R	RMSE	R	RMSE	R	RMSE	R	RMSE
Beijing	0.80	2.20	0.62	1.15	0.87	2.60	0.61	1.69	0.91	2.20	0.73	1.65
Tianjin	0.89	2.40	0.66	1.48	0.85	1.90	0.63	1.97	0.92	2.10	0.61	2.13
Shijiazhuang	0.77	2.80	0.52	2.02	0.82	2.50	0.66	1.69	0.88	2.20	0.58	1.95
Baoding	0.83	2.50	0.60	1.34	0.85	2.40	0.61	1.53	0.89	2.30	0.60	1.97
Handan	0.93	1.40	0.48	1.36	0.78	3.20	0.56	2.27	0.95	1.30	0.66	1.94
Tangshan	0.69	4.00	0.62	1.44	0.81	3.30	0.53	1.64	0.85	3.00	0.46	2.24
Cangzhou	0.85	3.00	0.64	1.23	0.79	2.50	0.60	1.92	0.94	2.10	0.75	1.45
Dezhou	0.78	3.70	0.51	1.69	0.87	1.50	0.63	2.82	0.90	2.30	0.55	2.97
Jinan	0.76	2.80	0.49	2.96	0.74	2.40	0.63	2.45	0.91	2.10	0.56	3.10
Weifang	0.79	2.10	0.53	1.42	0.78	2.50	0.71	1.99	0.94	2.10	0.85	1.40
Binzhou	0.81	2.50	0.51	1.97	0.83	2.30	0.86	1.29	0.92	2.00	0.81	1.47
Chengde	0.75	5.10	0.47	2.06	0.63	6.50	0.47	2.60	0.84	3.70	0.56	1.74
Zhangjiakou	0.90	5.40	0.33	2.23	0.77	5.30	0.47	3.13	0.96	4.80	0.54	2.50
Average	**0.81**	**3.07**	**0.54**	**1.72**	**0.80**	**2.99**	**0.61**	**2.08**	**0.91**	**2.47**	**0.64**	**2.04**

Case-1: west-southwest wind shear mode (January 17–21, 2018); Case-2: south-north wind shear mode (January 7–11, 2016); Case3: topographic obstruction category (October 7–12, 2014).

294
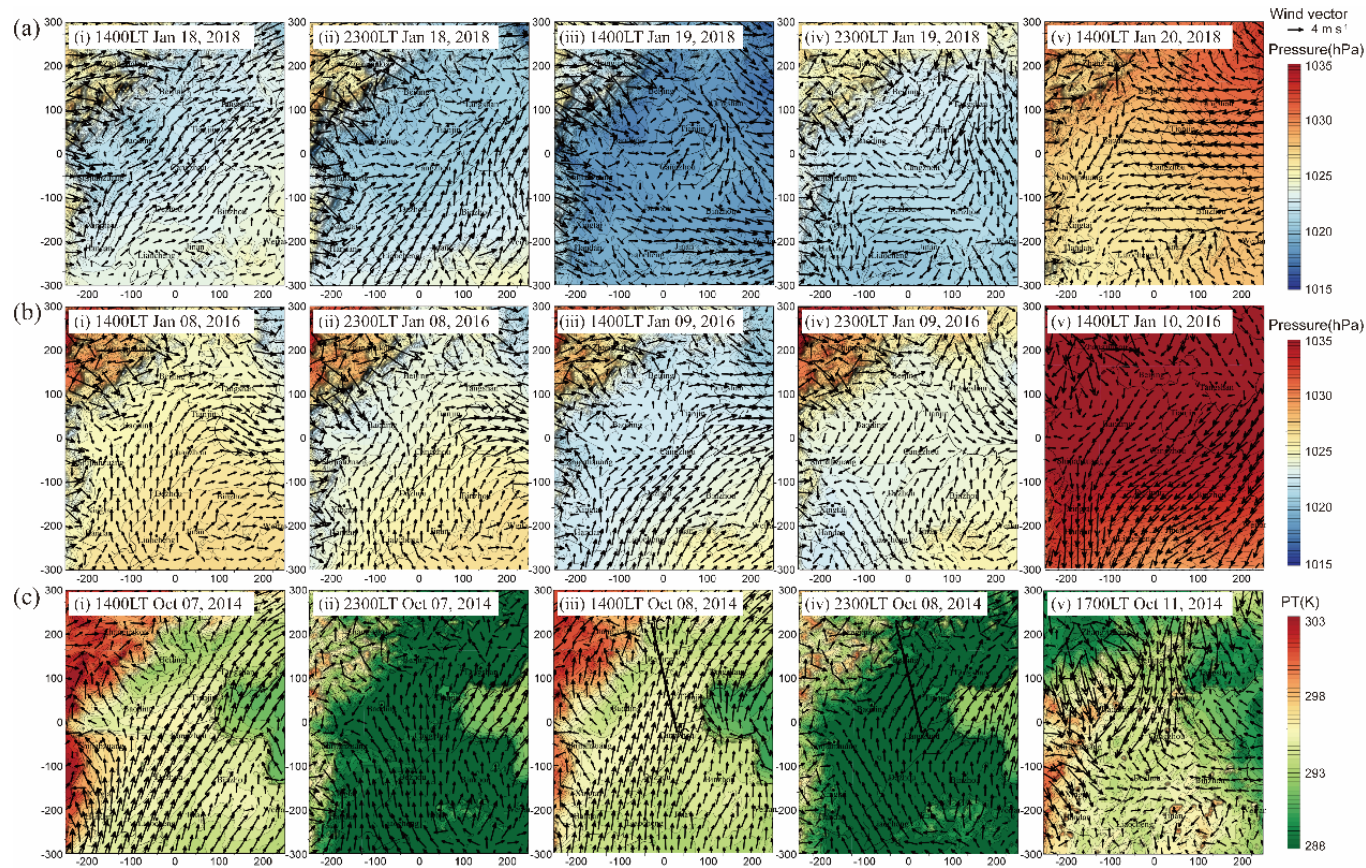
Figure 6. Simulated sea level pressure/potential temperature and wind vectors at the pollution stages of (i) formation, (ii-iv) maintenance, and (v) diffusion during representative

Case1–3 under (a) west-southwest wind shear mode, (b) south-north wind shear mode, and (c) topographic obstruction category. The shaded colors represent the sea level

pressure in (a-b) and the surface potential temperature in (c). The arrows indicate wind vectors. Values shown in x- and y-axis denote the distances (km) to the domain center.

Lines C_1C_1' in (c) refer to the cross-sections of the potential temperature in Fig. 11.

299   Compared with Fig. 5, the simulated surface meteorological fields during the three cases are

300   displayed in Fig. 6. In Case-1 and Case-2, the leeward trough and saddle-shaped pressure field, as well

301   as the corresponding west-southwest wind shear and south-north wind shear are reproduced in the

302   simulated fields (Fig. 6a-b, i-iv vs Fig. 5a-b, i-iv). Also, their movement and evolution during the

303   pollution formation-maintenance processes are captured by the WRF model, although there are small

304   deviations in the specific positions. At the diffusion stage, the simulated northeastern high-pressure and

305   the prevailing easterly/northeasterly winds are comparable with the observed fields (Fig. 6a-b, v vs Fig.

306   5a-b, v). As for Case-3, the modeling result of surface meteorological fields successfully reflect the

307   narrow cold zone and stagnant wind belt at the foot of the mountains, as well as their diurnal variation

308   and sustainability in the pollution formation-maintenance stage (Fig. 6c, i-iv vs Fig. 5c, i-iv). In the

309   simulation field, the cold zone is shorter at its south end on the afternoon of October 08, 2014, and there

310   is an overestimate of the potential temperature in the northwest mountains and the Bohai Sea at night. At

311   the end of this episode, a strong northerly cold airflow similar to the observation appears in the simulation

312   field (Fig. 6c, v vs Fig. 5c, v). Generally, the main features of the surface distributions of meteorological

313   observations during these three cases are reflected well in the simulated fields.

314   Moreover, the simulated and observed height-time cross sections of potential temperature and wind

315   speed, as well as the PBL height, are compared to reveal the model's ability to capture the atmospheric

316   vertical structure of each case (Fig. 7). The observation data of Case-1 and Case-2 are obtained from

317   intensive sounding experiments at the Dezhou site and Cangzhou site, respectively. While the observation

318   information during Case-3 is provided by routine soundings at the Beijing site. As for Case-1, the model

319   successfully reproduces the thermal structure evolution in the pollution formation-maintenance period,

320   while the final uplift of the inversion layer and the growth of PBL are not well captured with an

321   underestimation of about 200-300 m (Fig. 7a, i-ii). In comparison, the dynamic structures, the dominant

322   roles in this category, are simulated much better. The vertical location and temporal transition of the

323   strong and weak wind layers are comparable with observations (Fig. 7a, iii-iv). The correlation

324   coefficient (R) between simulated and observed PBL height is about 0.68 (p<0.01). The model

325   performance during Case-2 is satisfactory both for cross-sections of the potential temperature and wind

326   speed. The formation and decay of upper temperature inversion and the development of the cold

327   convective PBL are consistent between observation and simulation, though there are some

328   underestimations in the modeled results (Fig. 7b, i-ii). The weak wind layer presented in the maintenance

329   stage and vertical wind shear that occurred in the diffusion stage are also captured by the model with

330   smaller gradients (Fig. 7b, iii-iv). Meanwhile, observed and simulated PBL heights show a consistent

331   evolution with a correlation coefficient as high as 0.78 (p<0.01). Both of their PBL heights are lower

332   during the pollution formation-maintenance stage and increase by more than 1000 m in the diffusion

333   stage. In Case-3, the WRF reproduces the observed diurnal cycle of the potential temperature in the low-

level and the continuous warming at the upper layer during the formation-maintenance process, as well as the replacement of a well-mixed cold air mass in the last phase (Fig. 7c, i-ii). The evolution of the simulated wind speed is roughly similar to the observation, including the maintenance of the calm wind layer in the first four days and the appearance of the final strong wind layer (Fig. 7c, iii-iv). Correspondingly, the PBL height is characterized by typical diurnal variations during the polluted period, and begins to abruptly develop in the evening of October 12, 2014, associated with the cold air mass and strong wind, both in observation and simulation (R=0.81, p<0.01). Even so, there are some inconsistencies in the details of observation and simulation evolution, which may result from the coarse resolution of routine soundings in time and vertical direction, in addition to the uncertainties of model simulation.
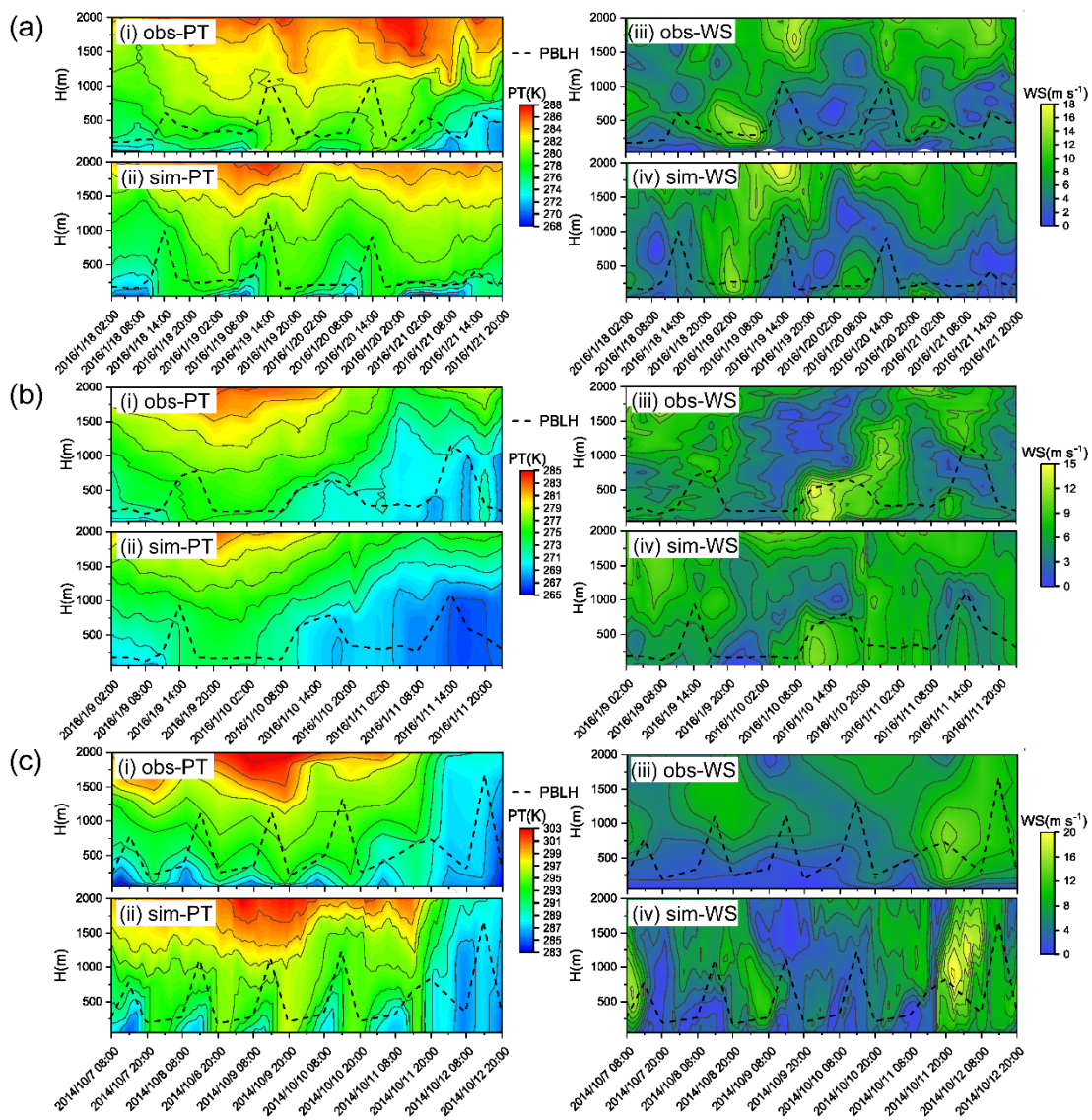
Figure 7. Observed and simulated time-height cross sections of potential temperature (left) and wind speed (right) during representative Case1–3 under (a) west-southwest wind shear mode (January 18–21, 2018), (b) south-north wind shear mode (January 9–11, 2016), and (c) topographic obstruction category

348 (October 7–12, 2014). The dashed lines indicate the PBL heights. The observation data in (a-b) and in

349 (c) are obtained from intensive sounding experiments and routine soundings, respectively.

350   Overall, the model shows the ability to capture the observed mesoscale systems and atmospheric

351 thermal-dynamic structures reasonably both at the surface and in the vertical direction. With confidence

352 in the model results, we now proceed to a detailed investigation of the PBL spatial structure affected by

353 mesoscale AIBs under various pollution categories.

354 **3.3 PBL spatial structure**

355   We analyze the simulated vertical cross-sections of the mesoscale systems and AIBs to reveal the

356 three-dimensional structure of the PBL. Two key parameters, potential temperature and wind divergence,

357 are used to respectively indicate the atmospheric thermal stability and dynamic convergence, in addition

358 to another important parameter: the PBL depth. They directly affect the vertical mixing and horizontal

359 diffusion of $PM_{2.5}$, and are critical for pollution formation and distribution.

360 **Wind shear category**

361   This pollution category, mainly involving two modes of west-southwest wind shear and south-north

362 wind shear, is driven by dynamic flows. Therefore, for the corresponding Case-1 and Case-2, the wind

363 divergence sections are analyzed in detail in the following (Figs. 8-9). The potential temperature sections

364 are presented in the supplementary material (Figs. S2-3), which illustrates that there is no significant

365 thermal discontinuity.

366   Figure 8 displays the PBL dynamic structure of Case-1. During the pollution formation-maintenance

367 stage, with the establishment of a low-pressure trough, westerly winds shifted to southwesterly winds at

368 the trough axis and thus formed a convergence belt at the surface with a divergence of $-2 \sim -4 \times 10^{-6}$ s^{-1}

369 (Fig. 8a, i). As a consequence, a mass of pollutants were transported here and further accumulated to

370 form a pollution zone (refer to Fig. 4a, i). This trough-convergence belt continued to move to the

371 southeast, and evolved into a cyclonic-convergence center at the end of the maintenance phase (Fig. 8a,

372 i-iv). During this process, its affected area was expanded, so that the large range of NCP was filled with

373 pollutants (refer to Fig. 4a, ii-iv). The vertical section across the surface convergence belt shows that the

374 depth of the convergence layer did not exceed 1000 m, with a compensating divergence layer

375 immediately above it, being consistent with the evolution of the PBL (Fig. 8b, i-iv). Furthermore, the

376 vertical profiles of the wind divergence and potential temperature at the Baoding site located in the

377 convergence belt are extracted to illustrate the PBL dynamic structure more clearly. It shows that the

378 mutation of divergence value and the jump of potential temperature roughly appeared at the same height

379 (Fig. 8c, i-iv), which demonstrated the vertical scale of the wind convergence belt was equivalent to the

380 depth of the PBL. This phenomenon reveals that the west-southwest wind convergence caused by the

381 trough mainly occurred within the PBL, reflecting its mesoscale property. In the process of pollution

diffusion, with the advent of a northeast high-pressure system, divergent wind fields occurred correspondently (Fig. 8a, v), which made this part of the pollutants cleaned quickly (refer to Fig. 4a, v). The vertical cross-section of this divergent layer and vertical profiles at the Tangshan site show that the northeast wind divergence layer was relatively thin with a thickness of no more than 600 m (Fig. 8b-c, v), implying that the removal of pollutants only occurred within the PBL.

As for the south-north wind shear mode, the surface divergence fields displayed a "lying Y shaped" convergence zone with the opening to the west during the pollution formation-maintenance stage of Case-2 (Fig. 9a, i-iv), which was caused by the meeting of the southerly winds and the northerly winds and then turning to the easterly winds. This convergence mode made the distribution of pollutants in a pattern of much higher concentration in the south and lower in the north, with a clear edge between these two air masses (refer to Fig. 4b, i-iv). Although the southerly winds in the southern NCP kept the pollutants transported northward, they never reached the northernmost part due to the opposite airflow there. The vertical cross-sections of this special convergence zone exhibited a depth extending upwards for more than 3000 m, with a peak between 1000 m and 2000 m above the PBL top (Fig. 9b, i-iv). Referring to the vertical profiles of wind divergence and potential temperature at the Baoding site, it can be seen that the depth of the convergence layer far exceeded the height of the PBL, whether it was in the daytime or at night (Fig. 9c, i-iv). These phenomena demonstrate that the south-north wind shear created by the saddle-shaped pressure field is of much larger vertical and horizontal scales. The dynamic feature was no longer limited to the PBL, but extended to the sub-synoptic scales. In the pollution diffusion stage of this case, the PBL structure was the same as in Case-1 (Fig. 9a-c, v), and has been described in the above paragraph.
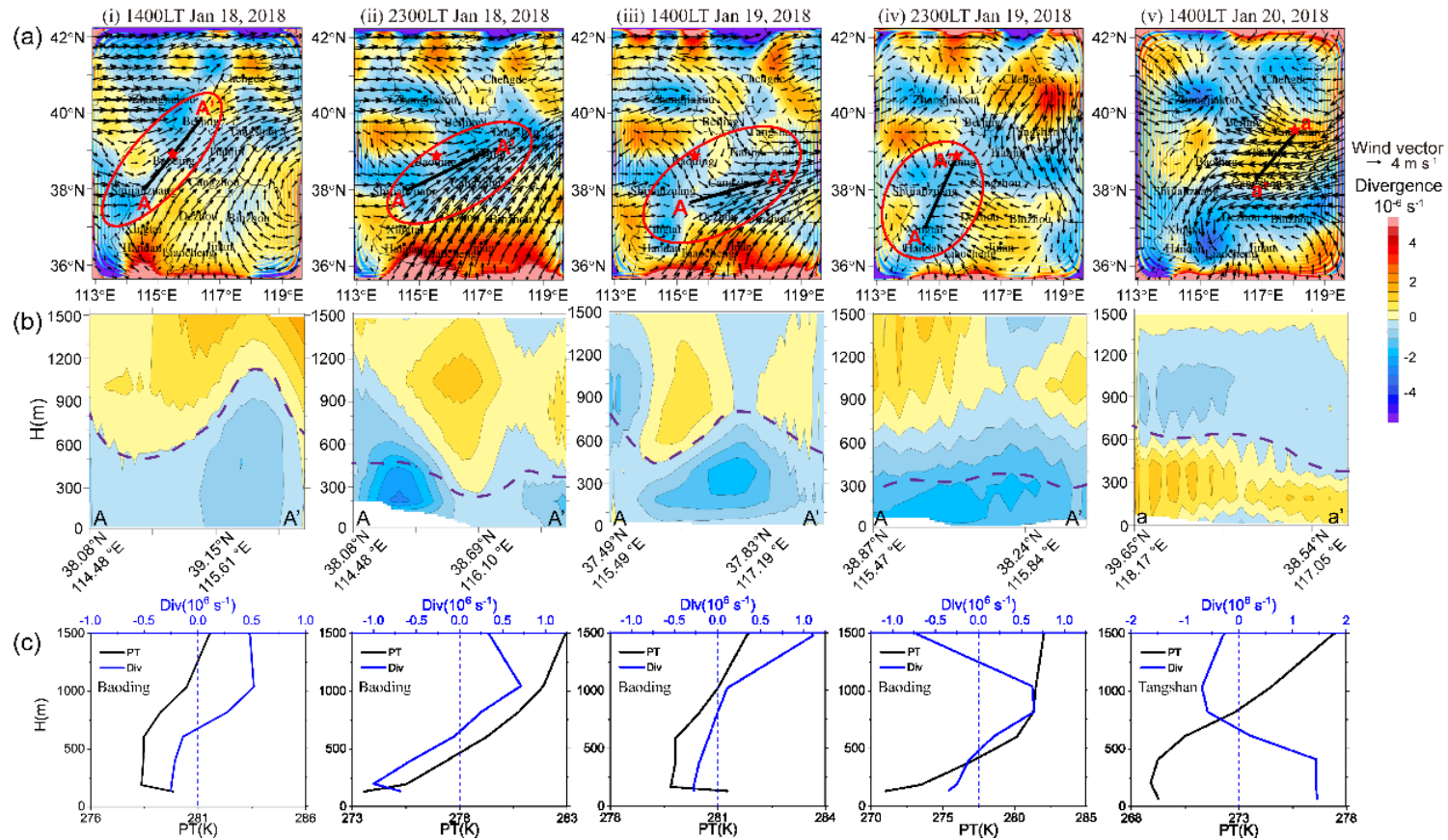
403
404 Figure 8. (a) Surface spatial distributions, (b) vertical cross-sections and (c) vertical profiles of the simulated wind divergence at the pollution stages of (i) formation, (ii-iv)
405 maintenance, and (v) diffusion during representative Case-1 under west-southwest wind shear mode. The red ellipses, black lines, and red stars in (a) indicate the convergence
406 belt, the section lines in (b), and the profile sites in (c), respectively. The purple dashed lines in (b) indicate the PBL heights. The potential temperature profiles are presented
407 in (c) to indicate the boundary layer top at the representative sites.
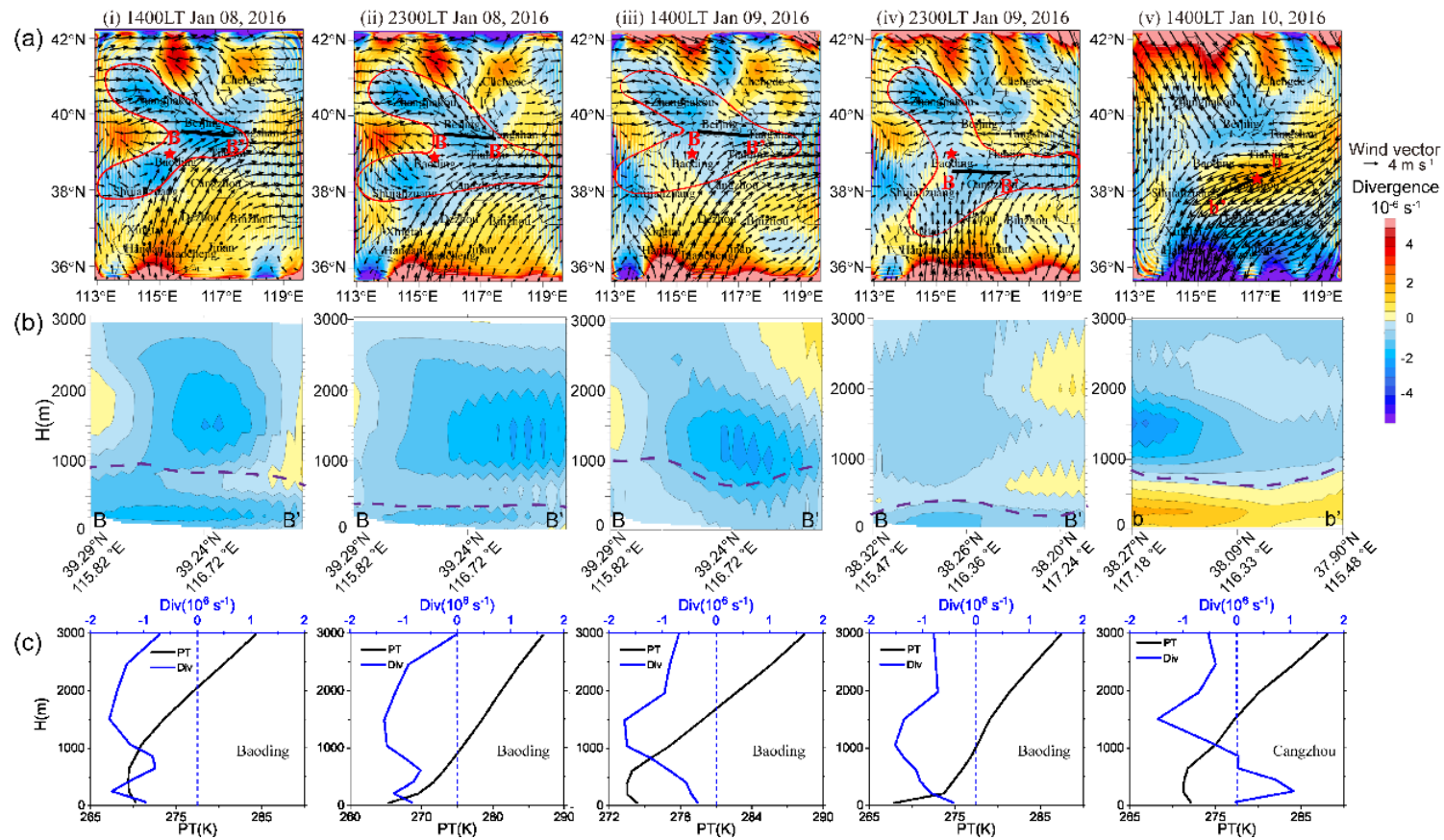
Figure 9. Same as Fig. 8, but for representative Case-2 under south-north wind shear mode. The red lying-Y shapes, black lines, and red stars in (a) indicate the convergence belt, the section lines in (b), and the profile sites in (c), respectively. The purple dashed lines in (b) indicate the PBL heights. The potential temperature profiles are presented in (c) to indicate the boundary layer top at the representative sites.

Topographic obstruction category

As an outcome of a mixture of the thermal and dynamic effects, the topographic obstruction category pollution is analyzed from the perspectives of both the wind divergence and potential temperature to reveal the thermal and dynamic structure of the PBL.

Figure 10 shows the dynamic characteristics of the PBL during Case-3. In the pollution formation-maintenance stage, there was an arc-shaped convergence belt at the foot of the mountains on the windward, due to the momentum loss in the northward flow under the action of topographic obstruction (Fig. 10a, i-iv). The shape of this convergent belt was more regular at night (Fig. 10a, ii, iv) but had some breakages at the northern edge during the day when there was a local southeast wind around Beijing and Shijiazhuang (Fig. 10a, i, iii). The vertical sections also displayed the general features and diurnal difference, showing an integral convergence layer at night with a depth of the mountain height (Fig. 10b, ii, iv), and an isolated divergent layer emerged during the daytime (Fig. 10b, i, iii). The vertical profiles of the wind divergence and potential temperature at Beijing were further shown in Fig. 10c, i-iv. In the evening, the atmosphere below 1200 m was convergent with the peak appearing near the surface of about -1.5×10^{-6} s^{-1}. In the afternoon, there was a weak divergence layer with a strength of about 0.5×10^{-6} s^{-1} and a thickness of about 200~300 m within the PBL. We infer that the day-night variation may be the consequence of the mountain-valley circulation, since the northwestward daytime valley winds developed along the mountain gorges near Beijing and Shijiazhuang leading to flow divergence, and downslope winds formed at night strengthening the surface convergence. During the pollution diffusion stage, the northern part of the domain was in a strong divergence condition (Fig. 10a, v). The corresponding cross-section shows that the north wind divergence layer was very deep (nearly 3000 m), even extending beyond the boundary layer. It gradually thins from north to south with the decrease of the PBL height (Fig. 10b, v). Moreover, the vertical profiles of the divergence and potential temperature at the Beijing site show that the PBL was well developed up to 2000 m, accompanied by strong horizontal divergence throughout the layer (Fig. 10c, v). Both of them indicate extremely favorable ventilation conditions.

438
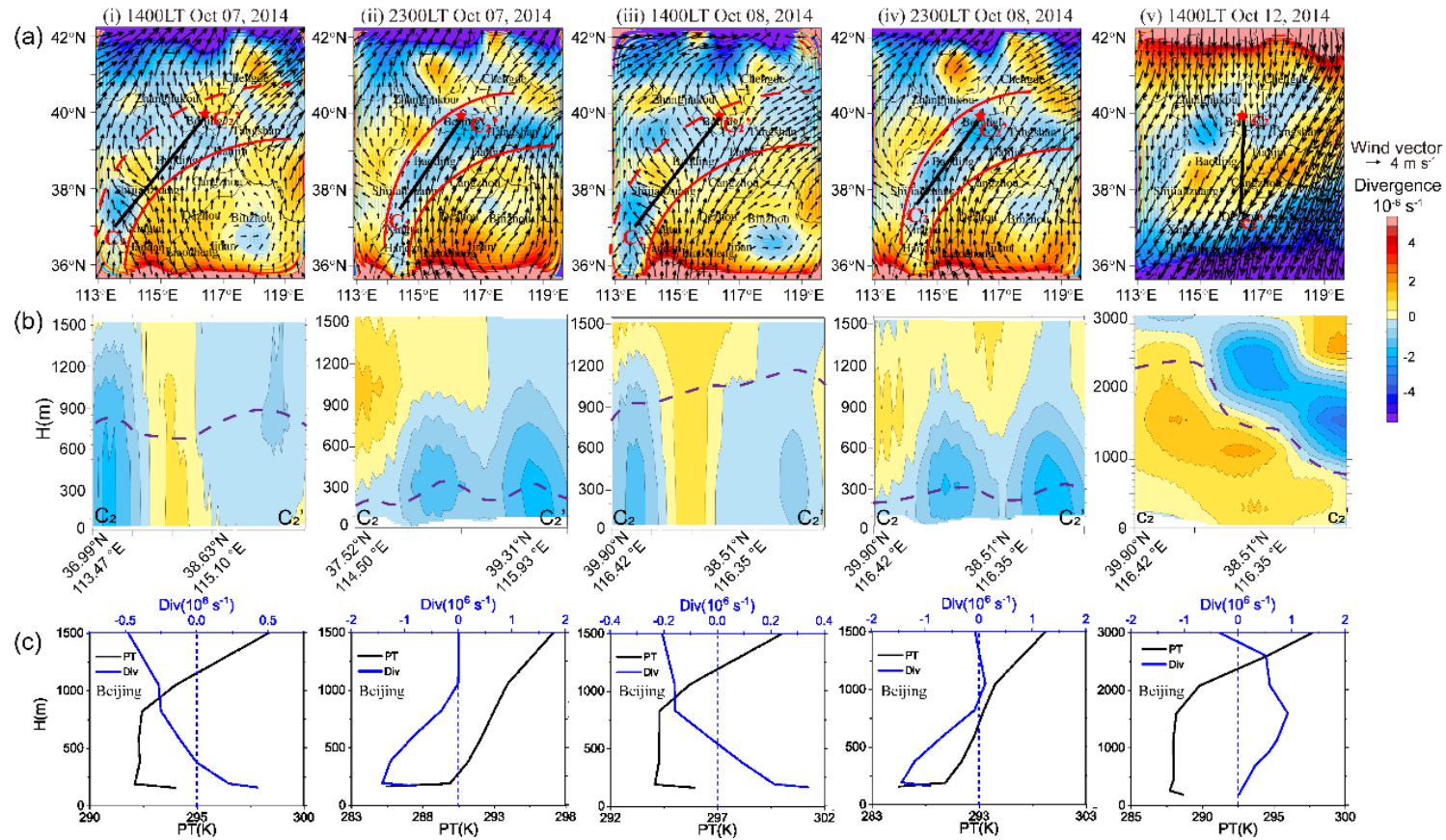
Figure 10. Same as Fig. 8, but for representative Case-3 under the topographic obstruction category. The red curves, black lines, and red stars in (a) indicate the convergence

440 belt, the section lines in (b), and the profile sites in (c), respectively. The purple dashed lines in (b) indicate the PBL heights. The potential temperature profiles are presented

441 in (c) to indicate the boundary layer top at the representative sites.

The thermal properties and their evolution, especially diurnal variation, play an important role in this pollution pattern, which has been presented in the above surface analysis. Hence, we further explore the three-dimension thermal structure of the PBL, taking the vertical cross-sections of potential temperature across the characteristic cold area in the pollution maintenance stage (October 8, 2014, the location of the cross-section is shown in Fig. 6c) as an illustration. In the early hours of the morning, although there were surface inversions across the whole region, the cold air masses in front of the mountains were much thicker (Fig. 11a, i). After sunrise, the convective boundary layer developed both in the front of the mountains and in the plain due to the surface heating, but the temperature in the southern plain was higher and the PBL was slightly deeper (Fig. 11a, ii). In the afternoon, a deep, well-mixed warm PBL (with a height of more than 1000 m) has formed in the southern plain while a cold air mass capped by strong inversion (at the height of about 600-1000 m) still remained in the northern piedmont area (Fig. 11a, iii). At night, large amounts of cold air accumulated at the foot of the mountains again (Fig. 11a, iv). The vertical profiles of the simulated potential temperature of the three cities from south to north, Jinan, Cangzhou and Beijing, also support this thermal evolution process. At 0200 LT, there were surface inversions at all three cities, and Beijing had the strongest inversion intensity of about 2 K per 100 m (Fig. 11b, i). By 1000 LT, the PBL height in Jinan had increased to 1100 m, while the convective boundary layers in Beijing and Cangzhou were shallow (about 400 m, Fig. 11b, ii). In the afternoon, the PBL was fully developed with the height from the south to the north site ranging from 1150 m to 650 m, and there was still a thick inversion layer above Beijing (Fig. 11b, iii). At 2300 LT, the surface inversion at the three sites has formed again (Fig. 11b, iv). The persistent cold air mass in front of the mountains is similar to the cold air damming on the eastern side of the Appalachian (Bell and Bosart, 1988). The prevailing southerly warm airflows were blocked by the mountains and the geostrophic balance was disrupted, so that the heat cannot reach the foothills and the air was further cooled due to the turning easterly wind. Meanwhile, the air mass accumulated and ascended with adiabatic cooling in front of the mountains. It should be noted that the southeast edge of this cold area was more pronounced during the daytime (Fig. 5c, Fig. 11), in comparison to that at night. This is reasonable given that the nocturnal boundary layer was stable over the whole domain and more susceptible to the local property, such as surface heterogeneity, meandering motions, and gravity waves (Mahrt, 1998). Although the AIB was relatively unclear at the surface during nighttime, the nocturnal cold layer at the foothills was deeper than the southern plain area, probably due to the cold drainage flows along the sidewall of the mountains to form a cold air pool. This diurnal cycle of the PBL thermal structure can well explain the day-night difference in pollution distribution pattern (refer to Fig. 4e).
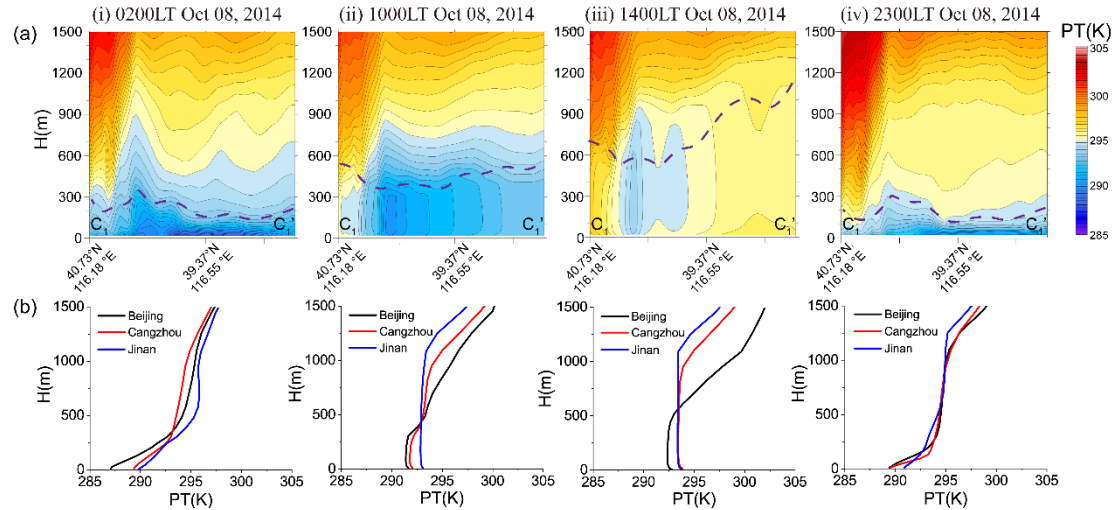
Figure 11. (a) Vertical cross-sections and (b) vertical profiles of the simulated potential temperature at (i) 0200 LT, (ii) 1000 LT, (iii) 1400 LT and (iv) 2300 LT on October 08, 2014 in Case-3 under the topographic obstruction category. The cross-sections along the line C_1C_1' are shown in Fig. 6c, iii, iv. The purple dashed lines in (a) indicate the PBL heights.

4 Summary and discussion

This study investigated the three-dimensional PBL structures modified by mesoscale AIBs under various pollution categories by using the mesoscale meteorological model WRF. Based on the classification of pollution episodes in the NCP (Jin et al., 2022 submitted), representative pollution cases of wind shear category and orographic obstruction category were analyzed. The WRF model was comprehensively evaluated for its reliability, by comparison with observed PBL vertical structure, as well as the temporal series and spatial distribution of the surface meteorological fields. The evolution of the PBL spatial structures and their interaction with the mesoscale AIBs during the pollution episodes were fully revealed, from both thermal and dynamic perspectives.

The results of this paper, together with a previous systematic classification study (Jin et al., 2022 submitted) and a detailed case study for frontal category (Jin et al., 2021), depict a more complete and clearer view of the PBL spatial structures during pollution episodes in the regional scale of NCP (as schematically shown in Fig.1). All the pollution conditions during the autumn and winter were classified into three categories. The most prominent was the frontal category. With an isolated cold air mass laterally bounded by the warm frontal AIB on one side and mountains on another side, the PBL was vertically suppressed by a dome-like warm cap. Typically, the intensity of the frontal inversion can be as large as 3~6 K per 100 m. As a consequence, the PBL in this cold area was very shallow (as low as 200~300 m) and kept stable stratification, in sharp contrast to the deep and well-mixing boundary layer outside this zone (Fig. 1a). This explained why $PM_{2.5}$ accumulated rapidly in this enclosed and stable

space and formed a laterally clearly defined polluted air mass. Diurnally, the nocturnal PBL in this category was less typical than its daytime counterpart. The thermal structure of the PBL played a leading role in this category, resulting in the most severe pollution level.

The wind shear category, with two main modes: west-southwest wind shear and south-north wind shear, was featured with airflow convergence AIB and dominated by dynamic processes. The first mode was characterized by a low-pressure trough. A convergence layer lay in the wind shear zone with the thickness of the PBL depth (Fig. 1b), and a typical near-surface divergence of $-2\sim-4\times10^{-6}$ s^{-1}. It is accompanied by a compensating divergence layer above the PBL, reflecting the mesoscale property of the trough AIB. The latter mode displayed a "lying Y shaped" convergence layer from the surface extending upwards to about 3000 m, with a convergence peak above the PBL top (not shown in Fig. 1). This implied the sub-synoptic scale features. In this category of both modes, the boundary layer was dominated by dynamic convergence effects, which resulted in pollutants transport and accumulation, and correspondent to relatively light pollution in the NCP.

The topographic obstruction pollution category was characterized by a cold air damming AIB at the foot of the windward side of the mountains. It usually occurred when the southerly winds were too weak to cross the terrain barrier and the northward flows were blocked. In response, the geostrophic balance was adjusted, which made the southerly warm advection weaken and further turned to easterly cold advection. All these factors allowed air masses to accumulate and ascend with adiabatic cooling at the foothills. The PBL air was cold and capped by a strong inversion in the damming area, in contrast with well-mixed warm PBL in the southern plain. Meanwhile, the air flows were convergent in front of the mountains. These general characteristics are shown in Fig. 1c. In more detail, the thermal discontinuity became indistinct at night due to the surface inversion over the whole domain, while the nocturnal wind convergence belt was more pronounced. The diurnal variation of the PBL dynamic and thermal structure made the pollutants concentrate at the foot of the mountains during the daytime while local pollution formed throughout the entire plain at night.

The present study focuses on the characteristic mesoscale PBL structures under pollution conditions, and emphasizes their role in shaping regional pollution patterns. The analysis of pollution evolution is based on the PM$_{2.5}$ concentration fields interpolated or diagnosed from monitoring data, relying on densely distributed stations. However, the PBL spatial structure is presented by numerical simulation, due to the scarcity and limitation of sounding data. Evaluation from the spatial-temporal variation of the surface meteorological field and PBL vertical structure indicates that the model performance is good. WRF can capture mesoscale systems and AIBs, as well as their overall evolution process and diurnal variation. It should be noted that, it is still difficult to reproduce the precise timing of the buildup and breakup as well as the exact location and range of these systems. This deficiency should be concerned seriously when simulated meteorological fields are used to drive air quality models, since a small position

bias and time deviation of the AIBs can significantly alter pollution levels at a certain site (Seaman, 2000; McNider and Pour-Biazar, 2020). Accurate capture of mesoscale AIBs is a necessary prerequisite for reliable simulation of pollution evolution. Besides, successful reproduction and forecast of air quality by the chemical transport models also involves other factors, such as the accuracy of source inventories and the complexity of chemical mechanisms (Travis et al., 2016; Bouarar et al., 2019; Wang et al., 2021), which are beyond the scope of this study. The aim of the present work is to provide a clear cognition of these typical PBL structures reproduced by numerical simulations. This goal is achieved satisfactorily.

At last, the pollution categories presented in this study can still be rough or oversimplified, and the real processes may be more complex and atypical as analyzed. However, this work, to the authors' knowledge, is the first trial to reveal the various PBL structures over the vast scale of the NCP, and to clarify their role in regional $PM_{2.5}$ pollution. Modulation of the PBL by mesoscale meteorological processes, particularly the AIBs, is clearly demonstrated. Extending the view of the PBL from local vertical properties to mesoscale three-dimension structures may be a step toward a better understanding of the meteorological effects on regional-scale $PM_{2.5}$ pollution.

Data availability

The data in this study are available from the corresponding author (xhcai@pku.edu.cn).

Author contribution

XHC and XPJ designed the research. MYY and HSZ collected the data. XPJ performed the simulations and wrote the paper. XHC reviewed and commented on the paper. YS, XSW and TZ participated in the discussion of the article.

Competing interests

The authors declare that they have no conflict of interest.

Acknowledgements

The authors appreciate the anonymous reviewers for the critical comments that have helped improve this manuscript. This work was supported by National Key Research and Development Program of China (2018YFC0213204).

References

Baumann, K., Maurer, H., Rau, G., Piringer, M., Pechinger, U., Prevot, A., Furger, M., Neininger, B. and Pellegrini, U.: The influence of south Foehn on the ozone distribution in the Alpine Rhine valley - results from the MAP field phase, Atmos. Environ., 35(36), 6379-6390, doi:10.1016/s1352-2310(01)00364-8, 2001.

Bei, N. F., Zhao, L. N. Wu, J. R., Li, X., Feng, T. and Li, G. H.: Impacts of sea-land and mountain-valley circulations on the air pollution in Beijing-Tianjin-Hebei (BTH): A case study, Environ. Pollut., 234, 429-438, doi:10.1016/j.envpol.2017.11.066,2018.

Bell, G. D. and Bosart, L. F.: Appalachian cold-air damming. Mon. Wea. Rev., 116, 137–161, doi:10.1175/1520-0493(1988)116,0137:ACAD.2.0.CO;2, 1988.

Berger, B. W. and Friehe, C. A.: Boundary-layer structure near the cold-front of a marine cyclone during "ERICA", Bound.-Layer Meteor., 317-317, doi:10.1007/BF0071125874, 1995.

Bluestein, H. B.: Surface boundaries of the Southern Plains: Their role in the initiation of convective storms, in: Synoptic-dynamic meteorology and weather analysis and forecasting: a tribute to Fred Sanders, edited by Bosart, L.F., Bluestein, H.B., American Meteorological Society, Boston, pp5-33, 2008.

Bianco, L., Djalalova, I. V., King, C. W., and Wilczak, J. M.: Diurnal Evolution and Annual Variability of Boundary-Layer Height and Its Correlation to Other Meteorological Variables in California's Central Valley, Bound.-Layer Meteor., 140, 491-511, doi:10.1007/s10546-011-9622-4, 2011.

Bouarar, I., Brasseur, G., Petersen, K., Granier, C., Fan, Q., Wang, X.M., Wang, L.L., Ji, D. S., Liu, Z.R., Xie, Y., Gao, W., and Elguindi, N.: Influence of anthropogenic emission inventories on simulations of air quality in China during winter and summer 2010. Atmos. Environ. 198, 236–256. https://doi.org/10.1016/j.atmosenv.2018.10.043, 2019.

Boutle, I. A., Beare, R. J., Belcher, S. E., Brown, A. R., and Plant, R. S.: The Moist Boundary Layer under a Mid-latitude Weather System, Bound.-Layer Meteor., 134, 367-386, doi:10.1007/s10546-009-9452-9, 2010.

De Wekker, S. F. J.: Observational and numerical evidence of depressed convective boundary layer heights near a mountain base, J. Appl. Meteorol. Climatol., 47, 1017-1026, doi:10.1175/2007jamc1651.1, 2008.

Dupont, J. C., Haeffelin, M., Badosa, J., Elias, T., Favez, O., Petit, J. E., Meleux, F., Sciare, J., Crenn, V., Bonne, J. L.: Role of the boundary layer dynamics effects on an extreme air pollution event in Paris. Atmos. Environ., 141, 571–579, doi:10.1016/j.atmosenv.2016.06.061, 2016.

Emeis, S., and Schafer, K.: Remote sensing methods to investigate boundary-layer structures relevant to air pollution in cities, Bound.-Layer Meteor., 121, 377-385, doi:10.1007/s10546-006-9068-2, 2006.

Garratt, J. R: The Atmospheric Boundary Layer. Cambridge University Press, Cambridge, 1992.

595 Garratt, J. R.: The internal boundary-layer-A review, Bound.-Layer Meteor., 50, 171-203,
596   doi:10.1007/bf00120524, 1990.

597 Hane, C. E., Rabin, R. M., Crawford, T. M., Bluestein, H. B. and Baldwin, M. E.: A case study of severe
598   storm development along a dryline within a synoptically active environment. Part II: Multiple
599   boundaries and convective initiation. Mon. Wea. Rev., 130, 900–920, doi: 10.1175/1520-
600   0493(2002)130<0900:ACSOSS>2.0.CO;2,2002.

601 Hanna, S. R. and Yang, R.: Evaluations of mesoscale models' simulations of near-surface winds,
602   temperature gradients, and mixing depths. J. Appl. Meteorol. 40 (6):1095–104, doi:10.1175/1520-
603   0450(2001)040<1095:EOMMSO>2.0.CO;2, 2001.

604 Jimenez, P. A., de Arellano, J. V. G., Dudhia, J., and Bosveld, F. C.: Role of synoptic- and meso-scales
605   on the evolution of the boundary-layer wind profile over a coastal region: the near-coast diurnal
606   acceleration, Meteorol. Atmos. Phys., 128, 39-56, doi:10.1007/s00703-015-0400-6, 2016.

607 Jin, X. P., Cai, X. H., Yu, M. Y., Song, Y., Wang, X. S., Kang, L. and Zhang, H. S.: Diagnostic analysis
608   of wintertime PM2.5 pollution in the North China Plain: The impacts of regional transport and
609   atmospheric boundary layer variation. Atmos. Environ., 224, 117346, doi:
610   10.1016/j.atmosenv.2020.117346, 2020.

611 Jin, X. P., Cai, X. H., Yu, M. Y., Wang, X. B., , Song, Y., Wang, X. S., Zhang, H. S. and Zhu, T.: Regional
612   PM2.5 pollution confined by atmospheric internal boundaries in the North China Plain: Analysis
613   based on surface observations, Sci. Total Environ., (submitted), 2022.

614 Jin, X. P., Cai, X. H., Yu, M. Y., Wang, X. S., Song, Y., Kang, L., Zhang, H. S. and Zhu, T.: Mesoscale
615   structure of the atmospheric boundary layer and its impact on regional air pollution: A case study,
616   Atmos. Environ., 258, doi:10.1016/j.atmosenv.2021.118511, 2021.

617 Lareau, N.P., Crosman, E., Whiteman, C. D., Horel, J. D., Hoch, S.W., Brown, W.O.J. and Horst, T.W.:
618   The persistent cold-air pool study, Bull. Amer. Meteor. Soc., 94, 51-63, doi: 10.1175/BAMS-D-11-
619   00255.1, 2013.

620 Li, J., Sun, J. L., Zhou, M. Y., Cheng, Z. G., Li, Q. C., Cao, X. Y. and Zhang, J. J.: Observational analyses
621   of dramatic developments of a severe air pollution event in the Beijing area. Atmos. Chem. Phys.
622   18, 3919-3935, doi: 10.5194/acp-18-3919-2018, 2018.

623 Li, Q. H., Wu, B. G., Liu, J. L., Zhang, H. S., Cai, X. H. and Song, Y.: Characteristics of the atmospheric
624   boundary layer and its relation with PM2.5 during haze episodes in winter in the North China Plain.
625   Atmos. Environ. 223, 117265, doi:org/10.1016/j.atmosenv.2020.117265, 2020.

626 Liu, N., Zhou, S., Liu, C. S., and Guo, J. P.: Synoptic circulation pattern and boundary layer structure
627   associated with PM2.5 during wintertime haze pollution episodes in Shanghai, Atmos. Res., 228,
628   186-195, doi:10.1016/j.atmosres.2019.06.001, 2019.

629 Liu, S. and Liang, X. Z.: Observed diurnal cycle climatology of planetary boundary layer height, J.

630   Climate, 23(21), 5790–5809, doi:10.1175/2010jcli3552.1, 2010.

631   Lu, R. and Turco, R. P.: Air pollution transport in a coastal environment II: 3-dimension simulations over

632   Los-Angeles basin, Atmos. Environ., 29(13), 1499-1518, doi:10.1016/1352-2310(95)00015-q,

633   1995.

634   Lyu, W., Li, Y., Guan, D. B., Zhao, H. Y., Zhang, Q., and Liu, Z.: Driving forces of Chinese primary air

635   pollution emissions: an index decomposition analysis, Journal of Cleaner Production, 133, 136-144,

636   doi:10.1016/j.jclepro.2016.04.093,2016.

637   Mahrt, L.: Stratified atmospheric boundary layers and breakdown of models, Theoretical and

638   Computational Fluid Dynamics, 11, 263-279, doi:10.1007/s001620050093,1998.

639   Mayfield, J. A. and Fochesatto, G. J.: The Layered Structure of the Winter Atmospheric Boundary Layer

640   in the Interior of Alaska, J. Appl. Meteorol. Climatol., 52, 953-973, doi:10.1175/jamc-d-12-01.1,

641   2013.

642   McNider, R. T. and Pour-Biazar, A.: Meteorological modeling relevant to mesoscale and regional air

643   quality applications: a review, J. Air Waste Manage. Assoc., 70, 2-43,

644   doi:10.1080/10962247.2019.1694602, 2020.

645   Miao, Y. C. and Liu, S. H.: Linkages between aerosol pollution and planetary boundary layer structure

646   in China, Sci. Total Environ., 650, 288-296, doi:10.1016/j.scitotenv.2018.09.032, 2019.

647   Miao, Y. C., Hu, X. M., Liu, S. H., Qian, T. T., Xue, M., Zheng, Y. J. and Wang, S.: Seasonal variation of

648   local atmospheric circulations and boundary layer structure in the Beijing-Tianjin-Hebei region and

649   implications for air quality, J. Adv. Model. Earth Syst., 7(4), 1602-1626,

650   doi:10.1002/2015ms000522, 2015.

651   Narasimha, R., Sikka, D. R. and Prabhu, A.: The Monsoon Trough Boundary Layer. Indian Academy of

652   Sciences, 422 pp, 1997.

653   Peng, H. Q., Liu, D. Y., Zhou, B., Su, Y., Wu, J. M., Shen, H., Wei, J. S., and Cao, L.: Boundary-Layer

654   Characteristics of Persistent Regional Haze Events and Heavy Haze Days in Eastern China, Adv.

655   Meteorol., doi:10.1155/2016/6950154, 2016.

656   Petaja, T., Jarvi, L., Kerminen, V. M., Ding, A. J., Sun, J. N., Nie, W., Kujansuu, J., Virkkula, A., Yang,

657   X. Q., Fu, C. B., Zilitinkevich, S. and Kulmala, M: Enhanced air pollution via aerosol-boundary

658   layer feedback in China. Sci Rep 6, 6, doi:10.1038/srep18998, 2016.

659   Pielke, R. A. and Uliasz, M.: Use of meteorological models as input to regional and mesoscale air quality

660   models—Limitations and strengths. Atmos. Environ., 32(8):1455–66, doi:10.1016/S1352-

661   2310(97)00140-4, 1998.

662   Potty, K. V. J., Mohanty, U. C., and Raman, S.: Simulation of boundary layer structure over the Indian

663   summer monsoon trough during the passage of a depression, J. Appl. Meteorol., 40, 1241-1254,

664   doi:10.1175/1520-0450(2001)040<1241:soblso>2.0.co;2, 2001.

Prezerakos, N. G.: Lower tropospheric structure and synoptic scale circulation patterns during prolonged temperature inversions over Athens, Greece, Theor. Appl. Climatol., 60, 63-76, doi:10.1007/s007040050034, 1998.

Qu, K., Wang, X. S., Yan, Y., Shen, J., Xiao, T., Dong, H. B., Zeng, L. M. and Zhang, Y. H.: A comparative study to reveal the influence of typhoons on the transport, production and accumulation of O-3 in the Pearl River Delta, China, Atmos. Chem. Phys., 21, 11593-11612, doi:10.5194/acp-21-11593-2021, 2021.

Rajkumar, G., Saraswat, R. S., and Chakravarty, B.: Thermodynamic structure of the monsoon boundary-layer under the influence of a large-scale depression, Bound.-Layer Meteor., 68, 131-137, doi:10.1007/bf00712667, 1994.

Ren, Y., Zhang, H. S., Wei, W., Wu, B. G., Cai, X. H. and Song, Y.: Effects of turbulence structure and urbanization on the heavy haze pollution process, Atmos. Chem. Phys., 19, 1041-1057, doi:10.5194/acp-19-1041-2019, 2019.

Rogers, R. E., Deng, A. J., Stauffer, D. R., Gaudet, B. J., Jia, Y. Q., Soong, S. T. and Tanrikulu, S.: Application of the Weather Research and Forecasting Model for Air Quality Modeling in the San Francisco Bay Area, J. Appl. Meteorol. Climatol., 52, 1953-1973, doi:10.1175/jamc-d-12-0280.1,2013.

Sanders, F., and Doswell, C. A.: A case for detailed surface-analysis, Bull. Amer. Meteorol. Soc., 76(4), 505-521, doi:10.1175/1520-0477(1995)076<0505:acfdsa>2.0.co;2,1995.

Seaman, N. L. and Michelson, S. A.: Mesoscale meteorological structure of a high-ozone episode during the 1995 NARSTO-Northeast study, J. Appl. Meteorol., 39, 384-398, doi:10.1175/1520-0450(2000)039<0384:mmsoah>2.0.co;2, 2000.

Seaman, N. L.: Meteorological modeling for air-quality assessments. Atmos. Environ. 34 (12–14):2231–59, doi:10.1016/S1352-2310(99)00466-5., 2000.

Seibert, R.: South foehn studies since the ALPEX experiment, Meteorol. Atmos. Phys., 43, 91–103, doi:10.1007/BF01028112, 1990.

Sinclair, V. A., Belcher, S. E., and Gray, S. L.: Synoptic Controls on Boundary-Layer Characteristics, Bound.-Layer Meteor., 134, 387-409, doi:10.1007/s10546-009-9455-6, 2010.

Sinclair, V. A.: A 6-yr Climatology of Fronts Affecting Helsinki, Finland, and Their Boundary Layer Structure, J. Appl. Meteorol. Climatol., 52, 2106-2124, doi:10.1175/jamc-d-12-0318.1, 2013.

Stull, R.: An Introduction to Boundary Layer Meteorology. Springer, New York, 1988.

Talbot, C., Augustin, P., Leroy, C., Willart, V., Delbarre, H., and Khomenko, G.: Impact of a sea breeze on the boundary-layer dynamics and the atmospheric stratification in a coastal area of the North Sea, Bound.-Layer Meteor., 125, 133-154, doi:10.1007/s10546-007-9185-6, 2007.

Tennekes, H.: The atmospheric boundary layer. Phys. Today 27, 52–63, doi:10.1063/1.3128397, 1974.

Travis, K. R., Jacob, D. J., Fisher, J. A., Kim, P. S., Marais, E. A., Zhu, L., Yu, K., Miller, C. C., Yantosca, R. M., Sulprizio, M. P., Thompson, A. M., Wennberg, P. O., Crounse, J. D., St Clair, J. M., Cohen, R. C., Laughner, J. L., Dibb, J. E., Hall, S. R., Ullmann, K., Wolfe, G. M., Pollack, I. B., Peischl, J., Neuman, J. A., and Zhou, X. L.: Why do models overestimate surface ozone in the Southeast United States?, Atmos. Chem. Phys., 16, 13561-13577, doi:10.5194/acp-16-13561-2016,2016.

Wang, W. G., Liu, M. Y., Wang, T. T., Song, Y., Zhou, L., Cao, J. J., Hu, J. N., Tang, G. G., Chen, Z., Li, Z. J., Xu, Z. Y., Peng, C., Lian, C. F., Chen, Y., Pan, Y. P., Zhang, Y. H., Sun, Y. L., Li, W. J., Zhu, T., Tian, H. Z., and Ge, M. F.: Sulfate formation is dominated by manganese-catalyzed oxidation of SO2 on aerosol surfaces during haze events, Nat. Commun., 12, doi:10.1038/s41467-021-22091-6,2021.

Xiao, Z. S., Miao, Y. C., Du, X. H., Tang, W., Yu, Y., Zhang, X., and Che, H. Z.: Impacts of regional transport and boundary layer structure on the PM2.5 pollution in Wuhan, Central China, Atmos. Environ., 230, doi:10.1016/j.atmosenv.2020.117508, 2020.

Ye, X .X., Song, Y., Cai, X. H., Zhang, H. S.: Study on the synoptic flow patterns and boundary layer process of the severe haze events over the North China Plain in January 2013, Atmos. Environ. Times 124, 129–145. https://doi.org/10.1016/j. atmosenv.2015.06.011, 2016.

Zhang, Q., Zheng, Y. X., Tong, D., Shao, M., Wang, S. X., Zhang, Y. H., Xu, X. D., Wang, J. N., He, H., Liu, W. Q., Ding, Y. H., Lei, Y., Li, J. H., Wang, Z. F., Zhang, X. Y., Wang, Y. S., Cheng, J., Liu, Y., Shi, Q. R., Yan, L., Geng, G. N., Hong, C. P., Li, M., Liu, F., Zheng, B., Cao, J. J., Ding, A. J., Gao, J., Fu, Q. Y., Huo, J. T., Liu, B. X., Liu, Z. R., Yang, F. M., He, K. B., and Hao, J. M.: Drivers of improved PM2.5 air quality in China from 2013 to 2017, Proc. Natl. Acad. Sci. U. S. A., 116, 24463-24469, doi:10.1073/pnas.1907956116, 2019.

Zhang, Q. Q., Ma, Q., Zhao, B., Liu, X. Y., Wang, Y. X., Jia, B. X., and Zhang, X. Y.: Winter haze over North China Plain from 2009 to 2016: Influence of emission and meteorology, Environ. Pollut., 242, 1308-1318, doi:10.1016/j.envpol.2018.08.019, 2018.

Zhao, C. Wang, F., Y., Shi, X. Q., Zhang, D. Z., Wang, C. Y., Jiang, J. H., Zhang, Q., and Fan, H.: Estimating the Contribution of Local Primary Emissions to Particulate Pollution Using High-Density Station Observations, J. Geophys. Res.-Atmos., 124, 1648-1661, doi:10.1029/2018jd028888,2019.